Faye, A., Rodríguez-Martínez, J.A., Volokh, K.Y. (2017). Spherical void expansion in rubber-like materials: The stabilizing effects ofviscosity and inertia. International Journal of Non-Linear Mechanics, 92, pp. 118-126.

DOI: https://doi.org/10.1016/j.ijnonlinmec.2017.04.005

Spherical void expansion in rubber-like materials: the stabilizing effects of viscosity and inertia

Anshul Faye[a,*], J. A. Rodríguez-Martínez[b], K. Y. Volokh[a]

[a] *Faculty of Civil and Environmental Engineering, Technion, Israel*
[b] *Department of Continuum Mechanics and Structural Analysis, University of Carlos III of Madrid, Spain*

Abstract

Dynamic cavitation is known to be a typical failure mechanism in rubber-like solids. While the mechanical behaviour of these materials is generally rate-dependent, the number of theoretical and numerical works addressing the problem of cavitation using nonlinear viscoelastic constitutive models is scarce. It has been only in recent years when some authors have suggested that cavitation in rubber-like materials is a dynamic fracture process strongly affected by the rate-dependent behaviour of the material because of the large strains and strain rates that develop near the cavity. In the present work we further investigate previous idea and perform finite element simulations to model the dynamic expansion of a spherical cavity embedded into a rubber-like ball and subjected to internal pressure. To describe the mechanical behaviour of the rubber-like material we have used an experimentally calibrated constitutive model which includes rate-dependent effects and material failure. The numerical results demonstrate that inertia and viscosity play a fundamental role in the cavitation process since they stabilize the material behaviour and thus delay failure.

Keywords: Dynamic cavitation; Dynamic failure; Rubber-like materials; Viscosity; Inertia

*Corresponding author.
Email address: dr.anshul.faye@gmail.com (Anshul Faye)

1. Introduction

An isolated cavity/void inside a solid, subjected to load either at the cavity wall or at the remote field, expands rapidly after a critical load is reached. This phenomenon is referred to as cavitation instability. Cavitation is known to be a typical failure mechanism in solids. Experimental evidences of cavitation and fracture led by cavitation are available for different materials such as ductile metals, polymers, elastomers and biological tissues (Ashby et al., 1989, Cristiano et al., 2010, Faye et al., 2016, 2015, Gent and Lindley, 1959, Kundu and Crosby, 2009, Zimberlin et al., 2007). When the applied load (either at the cavity wall or at the remote field) is less than the critical load for cavitation, a new equilibrium configuration is reached after some expansion of the void. When the applied load is higher than the critical load, the void expands at finite velocity and ultimately leads to material failure. If the expansion velocity is high enough, dynamic effects become meaningful and the void growth is influenced by inertia. A large number of analytical and numerical studies have been devoted to the analysis of quasi-static and dynamic cavitation in a wide variety of materials (Abeyaratne and Horgan, 1985, Ball, 1982, Bassani et al., 1980, Buchely and Marañon, 2016, Cohen and Durban, 2013, Durban and Baruch, 1976, Durban and Fleck, 1997, Durban and Masri, 2004, Fond, 2001, Henao, 2009, Horgan and Polignone, 1995, Hou and Abeyaratne, 1992, Huang et al., 1991, Hunter and Crozier, 1968, Ortiz and Molinari, 1992, Rodríguez-Martínez et al., 2014, Singh et al., 2013, 2014, Steenbrink et al., 1997, Wright and Ramesh, 2008, Wu et al., 2003).

With growing applications of soft and biological materials, the study of cavitation phenomena in elastic solids has become increasingly important. In particular, the acclaimed review articles published by Gent (1990), Horgan and Polignone (1995) and Fond (2001) attracted the attention of the Solid Mechanics community to the problem of cavitation in rubber-like materials. More recently, one should highlight the work of López-Pamies et al. (2011,) who introduced a new theory to model static cavitation in elastomeric solids that considers

general 3D loading conditions and incorporates direct information of the underlying defects at which cavitation can initiate. Just one year ago, López-Pamies and co-workers (Lefèvre et al., 2015) pushed forward the cavitation problem in elastomers and showed the need of including damage/failure mechanisms in the analysis because rubber-like materials fail at large, but finite strains. A similar idea was developed by Lev and Volokh (2016) who used a constitutive model which incorporates failure for analyzing cavitation in rubber. Using various nonlinear elastic material models, Lev and Volokh (2016) demonstrated the interplay between elasticity and fracture in the development of the cavitation process.

Though most rubber-like materials are rate-dependent, there are not many theoretical and numerical works which consider viscoelastic constitutive models to analyze the dynamic cavitation problem. Last year, Cohen and Molinari (2015) presented a theoretical framework to investigate dynamic cavitation in viscoelastic incompressible materials modeled with an hereditary integral-type formulation. To facilitate analytical solutions, Cohen and Molinari (2015) considered two specific loading cases, namely, a sudden constant deformation and a deformation that increases at constant rate. Their objective was to provide closed-form expressions to measure the local viscoelastic properties of the rubber-like material through controlled relaxation experiments. Moreover, Kumar et al. (2016) just published a paper that presents new insights into the relevance of inertial and viscous dissipation effects on the onset of cavitation in rubber. They concluded that viscosity and dynamic effects increase the values of the applied loads at which cavitation occurs. In the present work, we further investigate previous ideas and approach, using finite element simulations in ABAQUS/Explicit, the canonical problem of a spherical void embedded at the center of an elastic ball and subjected to internal pressure. The elastic medium is modelled with a rate-dependent constitutive model which accounts for material failure using energy limiters (Aranda-Iglesias et al., 2016, Volokh, 2007, 2013). The finite element calculations confirm the results of Cohen and Molinari (2015) and Kumar et al. (2016) and show, systematically, the stabilizing effect

of viscosity and inertia.

An outline of the paper is as follows. Section 2 records the basic equations of a viscoelastic model which describes the rate-dependent response of Styrene Butadiene rubber within a wide range of strain rates. Section 3 reviews a classical analytical solution for the dynamic cavitation of a spherical void embedded into an incompressible elastic ball and subjected to internal pressure. Section 4 presents a finite element model developed in ABAQUS/Explicit to simulate dynamic expansion of a spherical cavity inserted in a *slightly* compressible viscoelastic ball. The finite element results are presented in section 5 and rationalized with the predictions of the theoretical model. The main conclusions of this research are presented in section 6.

2. Nonlinear viscoelasticity with energy limiters

In this section we summarize the formulation of nonlinear viscoelasticity with energy limiters developed by Aranda-Iglesias et al. (2016) which adapted the Eulerian constitutive framework for large inelastic deformations previously proposed by Volokh (2013).

2.1. Basic equations

Consider a material point that occupies position $\mathbf{X}$ in the reference configuration Λ_0 of a deformable body. The current position vector $\mathbf{x}$ in the deformed configuration Λ is given by $\mathbf{x} = \chi(\mathbf{X}, \mathrm{t})$, where χ is a bijective and twice continuously differentiable mapping. Deformation in the vicinity of the material point is described by the deformation gradient tensor $\mathbf{F}$

$$\mathbf{F} = \frac{\partial \mathbf{x}}{\partial \mathbf{X}}. \tag{1}$$

The linear and angular momentum balance take the following forms

$$\mathrm{div}\boldsymbol{\sigma} + \mathbf{b} = \rho \mathbf{a}, \tag{2}$$

$$\boldsymbol{\sigma} = \boldsymbol{\sigma}^{\mathrm{T}}, \tag{3}$$

where the divergence operator is calculated with respect to the current coordinates $\mathbf{x}$; $\boldsymbol{\sigma}$ is the Cauchy stress tensor; $\mathbf{b}$ is the body force per unit of current volume; ρ and $\mathbf{a}$ are the current mass density and acceleration vector, respectively.

The balance of linear momentum on the body surface $\partial\Lambda$ reads

$$\boldsymbol{\sigma}\mathbf{n} = \bar{\mathbf{t}}, \tag{4}$$

where $\bar{\mathbf{t}}$ is a prescribed traction per unit area of the surface with the unit outward normal $\mathbf{n}$.

Alternatively to (4), a surface boundary condition can be imposed on placements

$$\mathbf{x} = \bar{\mathbf{x}}, \tag{5}$$

where the barred quantity is prescribed on the surface $\partial\Lambda$.

The initial conditions are

$$\mathbf{x}(\mathrm{t} = 0) = \mathbf{x}_0, \ \mathbf{v}(\mathrm{t} = 0) = \mathbf{v}_0, \tag{6}$$

where $\mathbf{v}$ is the velocity vector and $\mathbf{x}_0$ and $\mathbf{v}_0$ are prescribed in Λ.

2.2. Constitutive framework

We assume that the *standard solid* rheological model underlies the constitutive equations, in which a nonlinear spring A is parallel to the consequently joined nonlinear spring and dashpot B, see Fig. 1.

We assume an additive decomposition of the strain energy function of the form

$$\psi(\mathbf{B}, \mathbf{B}_{\mathrm{B}}, \xi) = \psi_{\mathrm{A}}(\mathbf{B}, \xi) + \psi_{\mathrm{B}}(\mathbf{B}_{\mathrm{B}}, \xi), \tag{7}$$

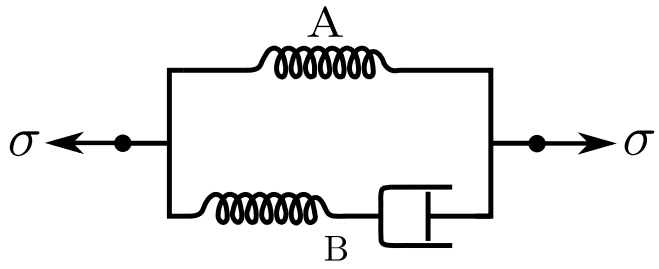

Figure 1: Rheological model for the *standard solid*.

where ψ_{A} is the strain energy function of spring A which serves to characterize the thermodynamic equilibrium states of the elastomer and ψ_{B} is the strain energy function of spring B which serves to account for the additional energy storage and non-equilibrium states. Furthermore, $\mathbf{B} = \mathbf{F}\mathbf{F}^{\mathrm{T}}$ is the left Cauchy-Green strain tensor, $\mathbf{B}_{\mathrm{B}}$ is an (strain like) internal variable of the model and ξ is a switch parameter (that will be defined later). We further impose the following conditions on the strain energy function of spring A

$$\psi_{\mathrm{A}}(\mathbf{B}, \xi) = \psi_{\mathrm{A}}^{\mathrm{f}} - \mathrm{H}(\xi)\psi_{\mathrm{A}}^{\mathrm{e}}(\mathbf{B}), \tag{8}$$

$$\psi_{\mathrm{A}}^{\mathrm{f}} = \psi_{\mathrm{A}}^{\mathrm{e}}(\mathbf{1}), \tag{9}$$

$$\| \mathbf{B} \| \to \infty \Rightarrow \psi_{\mathrm{A}}^{\mathrm{e}}(\mathbf{B}) \to 0, \tag{10}$$

where $\psi_{\mathrm{A}}^{\mathrm{f}}$ and $\psi_{\mathrm{A}}^{\mathrm{e}}(\mathbf{B})$ designate the constant bulk failure energy and the elastic free energy of spring A, respectively. Moreover, $\mathrm{H}(\xi)$ is a unit step function, i.e. $\mathrm{H}(z) = 0$ if $z < 0$ and $\mathrm{H}(z) = 1$ otherwise; $\mathbf{1}$ is a second-order identity tensor; and $\| \ldots \|$ is a tensor norm.

The switch parameter $\xi \in (-\infty, 0]$ is defined by the evolution equation

$$\dot{\xi} = -\mathrm{H}\left(\varepsilon - \frac{\psi_{\mathrm{A}}^{\mathrm{e}}}{\psi_{\mathrm{A}}^{\mathrm{f}}}\right), \quad \xi(\mathrm{t} = 0) = 0, \tag{11}$$

where $0 < \varepsilon \ll 1$ is a dimensionless precision constant. Note that a superposed dot denotes differentiation with respect to time.

The physical interpretation of the strain energy function is straightforward: the response of spring A is elastic as long as the strain energy is below its limit, $\psi_{\mathrm{A}}^{\mathrm{f}}$. When the limit is reached, the strain energy remains constant for the rest of the deformation process, thereby making material healing impossible. The parameter ξ is *not* an internal variable; it works as a switch: if $\xi = 0$ then the process is elastic and if $\xi < 0$ then the material is irreversibly damaged and the stored energy is dissipated.

In order to enforce the energy limiter in the strain energy function, we use the following form of the elastic energy

$$\psi_{\mathrm{A}}^{\mathrm{e}}(\mathbf{B}) = \frac{\Phi}{\mathrm{m}}\Gamma\left(\frac{1}{\mathrm{m}}, \frac{\mathrm{W_A}\left(\mathbf{B}\right)^{\mathrm{m}}}{\Phi^{\mathrm{m}}}\right), \tag{12}$$

where $\Gamma\left(\mathrm{s},\mathrm{x}\right) = \int_{\mathrm{x}}^{\infty} \mathrm{t}^{\mathrm{s}-1}\mathrm{e}^{-\mathrm{t}}\mathrm{dt}$ is the upper incomplete gamma function, $\mathrm{W_A}\left(\mathbf{B}\right)$ is the strain energy function of *intact* material, Φ is the energy limiter and m is a dimensionless material parameter which controls the sharpness of the transition to material failure in the stress-strain curve. Increasing or decreasing m it is possible to simulate more or less steep ruptures of the internal bonds accordingly.

The failure energy can be calculated as follows

$$\psi_{\mathrm{A}}^{\mathrm{f}} = \frac{\Phi}{\mathrm{m}}\Gamma\left(\frac{1}{\mathrm{m}}, \frac{\mathrm{W_A}\left(\mathbf{1}\right)^{\mathrm{m}}}{\Phi^{\mathrm{m}}}\right). \tag{13}$$

Note that the failure energy is a constant that depends on the two failure parameters (Φ, m) through the gamma function. There is no need to limit the energy of spring B as long as the failure of spring A leads to overall failure. Therefore, we define the strain energy function for spring B as

$$\psi_{\mathrm{B}}(\mathbf{B}_{\mathrm{B}}, \xi) = \mathrm{H}(\xi)\mathrm{W_B}(\mathbf{B}_{\mathrm{B}}), \tag{14}$$

where $\mathrm{W_B}(\mathbf{B}_{\mathrm{B}})$ stands for the strain energy without failure. Note that this formulation is valid for any pair of strain energies $\mathrm{W_A}$ and $\mathrm{W_B}$ used to describe the intact behaviour of the material (see section 2.4).

Based on the additive decomposition of the strain energy function ψ, the Cauchy stress is given by

$$\boldsymbol{\sigma} = \boldsymbol{\sigma}_{\mathrm{A}} + \boldsymbol{\sigma}_{\mathrm{B}}, \tag{15}$$

where

$$\boldsymbol{\sigma}_{\mathrm{A}} = 2\mathrm{I}_3^{-1/2}\frac{\partial \psi_{\mathrm{A}}}{\partial \mathbf{B}}\mathbf{B} = 2\mathrm{I}_3^{-1/2}\left(\mathrm{I}_3\psi_3\mathbf{1} + \left(\psi_1 + \mathrm{I}_1\psi_2\right)\mathbf{B} - \psi_2\mathbf{B}^2\right), \tag{16}$$

$$\boldsymbol{\sigma}_{\mathrm{B}} = 2\mathrm{I}_{\mathrm{B}3}^{-1/2}\frac{\partial \psi_{\mathrm{B}}}{\partial \mathbf{B}_{\mathrm{B}}}\mathbf{B}_{\mathrm{B}} = 2\mathrm{I}_{\mathrm{B}3}^{-1/2}\left(\mathrm{I}_{\mathrm{B}3}\psi_{\mathrm{B}3}\mathbf{1} + \left(\psi_{\mathrm{B}1} + \mathrm{I}_{\mathrm{B}1}\psi_{\mathrm{B}2}\right)\mathbf{B}_{\mathrm{B}} - \psi_{\mathrm{B}2}\mathbf{B}_{\mathrm{B}}^2\right). \tag{17}$$

The principal invariants are

$$\mathrm{I}_1 = \mathrm{tr}\mathbf{B}, \quad 2\mathrm{I}_2 = \left(\mathrm{tr}\mathbf{B}\right)^2 - \mathrm{tr}(\mathbf{B}^2), \quad \mathrm{I}_3 = \mathrm{det}\mathbf{B}, \tag{18}$$

$$\mathrm{I}_{\mathrm{B}1} = \mathrm{tr}\mathbf{B}_{\mathrm{B}}, \quad 2\mathrm{I}_{\mathrm{B}2} = \left(\mathrm{tr}\mathbf{B}_{\mathrm{B}}\right)^2 - \mathrm{tr}(\mathbf{B}_{\mathrm{B}}^2), \quad \mathrm{I}_{\mathrm{B}3} = \mathrm{det}\mathbf{B}_{\mathrm{B}}, \tag{19}$$

where $\psi_{\mathrm{i}} = \partial\psi/\partial\mathrm{I}_{\mathrm{i}}$ and $\psi_{\mathrm{Bi}} = \partial\psi/\partial\mathrm{I}_{\mathrm{Bi}}$.

The constitutive law (flow rule) for the dashpot is written in the following general form

$$\boldsymbol{\sigma}_{\mathrm{B}} = \beta_1\mathbf{1} + \beta_2\mathbf{D}_{\mathrm{B}} + \beta_3\mathbf{D}_{\mathrm{B}}^2, \tag{20}$$

where β_{s} are function(al)s, generally, depending on stresses and strains and $\mathbf{D}_{\mathrm{B}}$ is the rate of deformation tensor corresponding to the dashpot. Note that, as demonstrated by Aranda-Iglesias et al. (2016), the second law of thermodynamics requires that the following relation is fulfilled

$$\beta_1\mathbf{D}_{\mathrm{B}} + \beta_2\mathbf{D}_{\mathrm{B}}^2 + \beta_3\mathbf{D}_{\mathrm{B}}^3 \geq 0. \tag{21}$$

Following Eckart (1948), Leonov (1976) and Volokh (2013) the relation between $\mathbf{B}_{\mathrm{B}}$ and $\mathbf{D}_{\mathrm{B}}$ can be written as follows

$$\overset{\triangledown}{\mathbf{B}}_{\mathrm{B}} + \mathbf{D}_{\mathrm{B}}\mathbf{B}_{\mathrm{B}} + \mathbf{B}_{\mathrm{B}}\mathbf{D}_{\mathrm{B}} = \mathbf{0}, \quad \mathbf{B}_{\mathrm{B}}(\mathrm{t}=0) = \mathbf{1}, \tag{22}$$

where

$$\overset{\triangledown}{\mathbf{B}}_{\mathrm{B}} = \dot{\mathbf{B}}_{\mathrm{B}} - \mathbf{L}\mathbf{B}_{\mathrm{B}} - \mathbf{B}_{\mathrm{B}}\mathbf{L}^{\mathrm{T}}, \tag{23}$$

is the Oldroyd objective rate of the (strain like) internal variable $\mathbf{B}_{\mathrm{B}}$. In the previous expression $\mathbf{L}$ refers to the velocity gradient tensor of the whole model.

2.3. Specialization to incompressible and compressible materials

In this section we specialize the constitutive model to incompressible and (slightly) compressible materials. The hypothesis of incompressibility is used in section 3 to show the analytical (classical) solution of the dynamic (spherical) cavitation problem. Compressibility of the material is taken into account in the numerical model presented in section 4.

2.3.1. Incompressible formulation

The incompressibility condition implies that $\det\mathbf{B} = 1$, $\det\mathbf{B}_{\mathrm{B}} = 1$ and $\mathrm{tr}\mathbf{D}_{\mathrm{B}} = 0$. With these constraints, the constitutive laws for the springs (16)-(17) are written as follows

$$\boldsymbol{\sigma}_{\mathrm{A}} = -\mathrm{p}_{\mathrm{A}}\mathbf{1} + 2\left(\psi_1 + \mathrm{I}_1\psi_2\right)\mathbf{B} - \psi_2\mathbf{B}^2, \tag{24}$$

$$\boldsymbol{\sigma}_{\mathrm{B}} = -\mathrm{p}_{\mathrm{B}}\mathbf{1} + 2\left(\psi_{\mathrm{B}1} + \mathrm{I}_{\mathrm{B}1}\psi_{\mathrm{B}2}\right)\mathbf{B}_{\mathrm{B}} - \psi_{\mathrm{B}2}\mathbf{B}_{\mathrm{B}}^2, \tag{25}$$

where p_{A} and p_{B} are undefined Lagrange multipliers enforcing incompressibility.

The constitutive law for the dashpot (20) can be written as

$$\beta_1 = \frac{1}{3}\mathrm{tr}\boldsymbol{\sigma}_{\mathrm{B}}, \quad \beta_2 = \eta_2, \quad \beta_3 = 0, \tag{26}$$

where η_2 is the only viscosity parameter (or function).

Substitution of (26) in (20) yields

$$\boldsymbol{\sigma}_{\mathrm{B}} = \frac{1}{3}\left(\mathrm{tr}\boldsymbol{\sigma}_{\mathrm{B}}\right)\mathbf{1} + \eta_2 \mathbf{D}_{\mathrm{B}}, \tag{27}$$

Moreover, the thermodynamic restriction requires that

$$\eta_2 \geq 0. \tag{28}$$

2.3.2. Compressible formulation

Implementation of strict incompressibility is difficult (and unnecessary) in numerical simulations. Hence the constitutive equations are modified by penalizing the incompressibility conditions with large bulk moduli to implement material compressibility. The constitutive laws for the springs are written as

$$\boldsymbol{\sigma}_{\mathrm{A}} = 2\mathrm{I}_3^{-1/2}\left((\mathrm{I}_3\mathrm{k}_1 - \mathrm{k}_2)\mathbf{1} + (\psi_1 + \mathrm{I}_1\psi_2)\,\mathbf{B} - \psi_2\mathbf{B}^2\right), \tag{29}$$

$$\boldsymbol{\sigma}_{\mathrm{B}} = 2\mathrm{I}_{\mathrm{B3}}^{-1/2}\left((\mathrm{I}_{\mathrm{B3}}\mathrm{k}_{\mathrm{B1}} - \mathrm{k}_{\mathrm{B2}})\mathbf{1} + (\psi_{\mathrm{B1}} + \mathrm{I}_{\mathrm{B1}}\psi_{\mathrm{B2}})\,\mathbf{B}_{\mathrm{B}} - \psi_{\mathrm{B2}}\mathbf{B}_{\mathrm{B}}^2\right), \tag{30}$$

where k_1, k_2 and k_{B1}, k_{B2} are the penalizing bulk moduli for springs A and B accordingly.

We note that the bulk moduli are not independent and they should obey the condition of zero stress for $\mathbf{B} = \mathbf{B}_{\mathrm{B}} = \mathbf{1}$ and $\mathbf{D} = \mathbf{0}$. Thus, we obtain the relations

$$\mathrm{k}_1 \approx \mathrm{k}_2 \gg \psi_1 + 2\psi_2, \quad \mathrm{k}_{\mathrm{B1}} \approx \mathrm{k}_{\mathrm{B2}} \gg \psi_{\mathrm{B1}} + 2\psi_{\mathrm{B2}}, \tag{31}$$

which allow to obtain slight compressibility in the numerical simulations.

The constitutive law for dashpot is specified in a simple form to reproduce the flow rule proposed by Reese and Govindjee (1998) as follows,

$$\beta_1 = \frac{3\eta_1 - 2\eta_2}{9\eta_1}\mathrm{tr}\boldsymbol{\sigma}_{\mathrm{B}}, \quad \beta_2 = \eta_2, \quad \beta_3 = 0, \tag{32}$$

where η_1, η_2 are two viscosity parameters (or functions). One of the major advantage of this flow rule is that it takes into account for the large deformations and hence it is suitable for rubber-like materials.

Substituting (32) in (20) yields

$$\boldsymbol{\sigma}_{\mathrm{B}} = \frac{3\eta_1 - 2\eta_2}{9\eta_1} \left(\mathrm{tr}\boldsymbol{\sigma}_{\mathrm{B}}\right) \mathbf{1} + \eta_2 \mathbf{D}_{\mathrm{B}}. \tag{33}$$

Moreover, the thermodynamic restriction requires that

$$\eta_2 \geq 0, \quad 3\eta_1 \geq 2\eta_2. \tag{34}$$

2.4. Material parameters

Following Aranda-Iglesias et al. (2016), we use the formulation proposed by López-Pamies (2010) for the intact strain energy functions

$$W_{\mathrm{A}}(\mathbf{B}) = \frac{3^{(1-\alpha_1)}}{2\alpha_1}\mu_1 \left(\mathrm{I}_1^{\alpha_1} - 3^{\alpha_1}\right) + \frac{3^{(1-\alpha_2)}}{2\alpha_2}\mu_2 \left(\mathrm{I}_1^{\alpha_2} - 3^{\alpha_2}\right), \tag{35}$$

and

$$W_{\mathrm{B}}(\mathbf{B}_{\mathrm{B}}) = \frac{3^{(1-\alpha_{\mathrm{B1}})}}{2\alpha_{\mathrm{B1}}}\mu_{\mathrm{B1}} \left(\mathrm{I}_{\mathrm{B1}}^{\alpha_{\mathrm{B1}}} - 3^{\alpha_{\mathrm{B1}}}\right) + \frac{3^{(1-\alpha_{\mathrm{B2}})}}{2\alpha_{\mathrm{B2}}}\mu_{\mathrm{B2}} \left(\mathrm{I}_{\mathrm{B1}}^{\alpha_{\mathrm{B2}}} - 3^{\alpha_{\mathrm{B2}}}\right). \tag{36}$$

The viscosity function is taken from Hoo Fatt and Ouyang (2008) and reads as follows

$$\eta_2 = \left(\mathrm{C}_1(1 - \exp(\mathrm{C}_2(\mathrm{I}_1 - 3))) + \mathrm{C}_3\right) \left(\mathrm{C}_4\mathrm{I}_{\mathrm{B1}}^3 + \mathrm{C}_5\mathrm{I}_{\mathrm{B1}}^2 + \mathrm{C}_6\mathrm{I}_{\mathrm{B1}} + \mathrm{C}_7\right). \tag{37}$$

The complete constitutive model has 17 parameters: 6 for spring A (μ_1, μ_2, α_1, α_2, m, Φ), 4 for spring B (μ_{B1}, μ_{B2}, α_{B1}, α_{B2}) and 7 for the dashpot (C_1, C_2, C_3, C_4, C_5, C_6, C_7). Aranda-Iglesias et al. (2016) calibrated the constitutive model to describe the mechanical behaviour of Styrene Butadiene rubber. Small particles of Styrene Butadiene rubber are added to a large number

of semi-crystalline brittle polymers to increase their toughness (Bucknall, 1977). In these rubber–modified polymers major source of toughening comes from the energy consumed by the deformation of rubber particles before they fail due to cavitation (Serpooshan et al., 2007). Due to higher toughness most of these polymers are used in impact applications. Thus study of cavitation in Styrene Butadiene rubber is important.

The values of the parameters are listed in Table 1. Moreover, the bulk moduli (k_2, k_2, k_{B1}, k_{B2}) take the value 10^3 MPa for all the numerical simulations reported in this paper. The material density is 900 kg/m^3.

Table 1: Material parameters for Styrene Butadiene rubber as taken from Aranda-Iglesias et al. (2016).

Spring A

μ_1 (MPa)	α_1	μ_2 (MPa)	α_2	m	Φ (MPa)
0.391	1.045	2.162	-3.065	30	7.5

Spring B

μ_{B1} (MPa)	α_{B1}	μ_{B2} (MPa)	α_{B2}
3.99	0.382	2.868	-11.295

Dashpot B

C_1 (MPa · s)	C_2	C_3 (MPa · s)	C_4	C_5	C_6	C_7
23.095	7.421×10^{-8}	-8.458×10^{-7}	-872.52	-7975.595	22150.457	27310.182

Note that, in agreement with the experimental evidence reported by Hoo Fatt and Ouyang (2008), the constitutive model captures the rate-independent response of the material at sufficiently low and high strain rates. In the quasi-static limit and for strain rates above $\approx 2000\ s^{-1}$ the branch B of the rheological model will exhibit *purely* elastic response.

3. Theoretical model

We present the main features of the analytical (classical) solution for the dynamic cavitation of a spherical void embedded in an incompressible elastic ball and subjected to internal pressure. Note that the material is taken as *purely* elastic, i.e. viscous effects are not accounted for. The analytical solution will be used in section 5 as a reference to rationalize the finite element results presented in section 5.

3.1. Radially symmetric dynamic deformations

If the material is deformed so that the spherical symmetry is maintained, the motion is given by

$$\mathrm{r} = \mathrm{r}(\mathrm{R}, \mathrm{t}),\ \theta = \Theta,\ \omega = \Omega, \tag{38}$$

where $(\mathrm{r}, \theta, \omega)$ denote the current coordinates of a point having coordinates $(\mathrm{R}, \Theta, \Omega)$ in the undeformed configuration. For the motion described in (38), the deformation gradient tensor is

$$\mathbf{F} = \frac{\partial \mathrm{r}}{\partial \mathrm{R}} \mathbf{e}_{\mathrm{r}} \otimes \mathbf{E}_{\mathrm{R}} + \frac{\mathrm{r}}{\mathrm{R}} \mathbf{e}_{\theta} \otimes \mathbf{E}_{\Theta} + \frac{\mathrm{r}}{\mathrm{R}} \mathbf{e}_{\omega} \otimes \mathbf{E}_{\Omega}, \tag{39}$$

where $(\mathbf{E}_{\mathrm{R}}, \mathbf{E}_{\Theta}, \mathbf{E}_{\Omega})$ and $(\mathbf{e}_{\mathrm{r}}, \mathbf{e}_{\theta}, \mathbf{e}_{\omega})$ are reference and current base vectors in standard spherical coordinate system, respectively. Moreover, the displacement of a material point is

$$\mathbf{u} = \mathrm{u}_{\mathrm{r}}(\mathrm{r}, \mathrm{t}) \mathbf{e}_{\mathrm{r}}, \tag{40}$$

where $\mathrm{u}_{\mathrm{r}}(\mathrm{r}, \mathrm{t}) = \mathrm{r}(\mathrm{t}) - \mathrm{R}$. Next, relying on the incompressibility condition, the velocity and acceleration of a material point are given as

$$\mathbf{v} = \dot{\mathbf{u}} = \dot{\mathrm{a}} \left(\frac{\mathrm{a}}{\mathrm{r}} \right)^2 \mathbf{e}_{\mathrm{r}}, \tag{41}$$

$$\dot{\mathbf{v}} = \left(\frac{2\mathrm{a}\dot{\mathrm{a}}^2 + \mathrm{a}^2 \ddot{\mathrm{a}}}{\mathrm{r}^2} - \frac{2\mathrm{a}^4 \dot{\mathrm{a}}^2}{\mathrm{r}^5} \right) \mathbf{e}_{\mathrm{r}}, \tag{42}$$

where $a = a(t)$ is the radius of the cavity in the current configuration. In the undeformed configuration this is denoted as $a_0 = a(0)$.

Moreover, the Eulerian form of the conservation of linear momentum along the radial direction is

$$\frac{d\sigma_{rr}}{dr} + \frac{2\left(\sigma_{rr} - \sigma_{\theta\theta}\right)}{r} = \rho_0 \dot{v}_r, \tag{43}$$

where ρ_0 is the (constant) material density and $\dot{v}_r$ denotes the radial acceleration.

The boundary conditions of the problem are

$$\sigma_{rr}(r = a) = -P(t), \qquad \sigma_{rr}(r = b) = 0, \tag{44}$$

where $P(t)$ is the pressure applied at the cavity wall. Note that $b = b(t)$ is the outer radius of the ball in the current configuration. In the undeformed configuration this will be denoted as $b_0 = b(0)$.

Substituting (42) in (43) and integrating the balance of linear momentum along the radial coordinate using the boundary conditions defined in (44), we get

$$P(t) = P^{Eq} + P^{Dyn}, \tag{45}$$

where

$$P^{Eq} = -\int_a^b \frac{2\left(\sigma_{rr} - \sigma_{\theta\theta}\right)}{r} dr, \tag{46}$$

and

$$P^{Dyn} = \rho_0 \left[\left(2\dot{a}^2 + a\ddot{a}\right)\left(1 - \frac{a}{b}\right) - \frac{\dot{a}^2}{2}\left(1 - \frac{a^4}{b^4}\right)\right]. \tag{47}$$

The first term in (45) is the pressure due to the elastic response and depends on the difference of the principal stresses. The second term in (45) is the pressure due to inertial effects and depends on the mas density ρ_0, the outer radius of the elastic ball b, the size of the cavity a and the velocity $\dot{a}$ and acceleration $\ddot{a}$ at which the cavity grows.

3.2. Non-viscous quasi-static bounds

The rate sensitivity of the viscoelastic material described in section 2 is restricted to a finite range of strain rates. As discussed in section 2.4, at sufficiently low and high strain rates the dashpot does not play any role in the response of the rheological model presented Fig. 1. The lower bound of the viscous regime corresponds to the mechanical response defined by spring A (only) and the upper bound to the joint response of springs A and B. Next, for the quasi-static case, we derive theoretical solutions for the lower and upper bounds that will be used to rationalize the finite element simulations reported in section 5.

- **Lower bound solution**

  Considering only spring A, the strain energy function becomes

$$\psi(\mathbf{B}) = \psi_{\mathrm{A}}(\mathbf{B}, \xi), \tag{48}$$

  which yields

$$\psi_1 = \mathrm{H}(\xi)\exp\left(-\frac{\mathrm{W}_{\mathrm{A}}^{\mathrm{m}}}{\Phi^{\mathrm{m}}}\right)\frac{\partial \mathrm{W}_{\mathrm{A}}}{\partial \mathrm{I}_1}. \tag{49}$$

- **Upper bound solution**

  Considering springs A and B, the strain energy function becomes

$$\psi(\mathbf{B}) = \psi_{\mathrm{A}}(\mathbf{B}, \xi) + \psi_{\mathrm{B}}(\mathbf{B}, \xi), \tag{50}$$

  which yields

$$\psi_1 = \mathrm{H}(\xi)\left[\exp\left(-\frac{\mathrm{W}_{\mathrm{A}}^{\mathrm{m}}}{\Phi^{\mathrm{m}}}\right)\frac{\partial \mathrm{W}_{\mathrm{A}}}{\partial \mathrm{I}_1} + \frac{\partial \mathrm{W}_{\mathrm{B}}}{\partial \mathrm{I}_1}\right]. \tag{51}$$

Using the definitions of σ_{rr} and $\sigma_{\theta\theta}$ given in (24) we obtain

$$\sigma_{rr} - \sigma_{\theta\theta} = 2\psi_1 \left(B_{rr} - B_{\theta\theta}\right). \tag{52}$$

Inserting (52) into (45) and neglecting the inertia term we obtain

$$P\left(t\right) = -\int_a^b 4\psi_1(I_1(r)) \left(\frac{R^4}{r^4} - \frac{r^2}{R^2}\right) \frac{dr}{r}, \tag{53}$$

with

$$I_1(r) = \frac{R^4}{r^4} + 2\frac{r^2}{R^2} \quad \text{and} \quad R(r,a) = \left(r^3 - a^3 + a_0^3\right)^{1/3}. \tag{54}$$

Replacing ψ_1 in (53) by (49) and (51) we obtain the lower bound P_{lower} and upper bound P_{upper} solutions for the static pressure, respectively. These are shown in Fig. 2 as a function of the normalized void radius a/a_0. We observe that P_{lower} and P_{upper} increase rapidly (and almost linearly) for short values of a/a_0 and saturate for large values of a/a_0. Within the whole range of values of a/a_0 explored, P_{lower} goes below P_{upper}, as expected. Critical pressures corresponding to unstable expansion of void are obtained as $P_{lower}^{cr} \approx 2$ MPa and $P_{upper}^{cr} \approx 9.5$ MPa. Failure at the cavity surface (r = a) will occur when material failure criteria discussed in Sec. 2 is satisfied. Note that, to obtain the solutions plotted in Fig. 2 we have used $b_0 = 1000a_0$. This ratio between the inner and outer radius of the elastic ball is large enough to make the solution virtually independent of b_0 (Volokh, 2007).

4. Numerical model

This section describes the features of the axisymmetric finite element model developed to simulate dynamic spherical cavity expansion. The numerical analyses are carried out using the finite element program ABAQUS/Explicit (ABAQUS/Explicit, 2013). The problem setting is of a very large sphere of radius $b_0 = 100$ mm with a small cavity in its center of radius a_0. Three values of a_0 are explored in the numerical calculations presented in section 5, namely 0.01, 0.1 and 1 mm. Due to the symmetry of the model, only the $\Theta \geq 0$ half of the specimen has

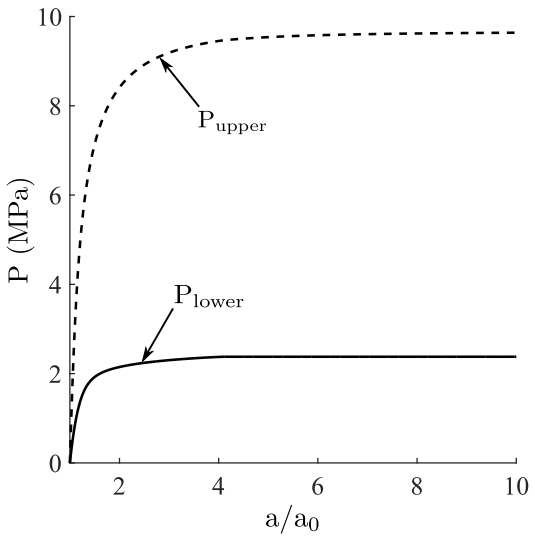

Figure 2: Lower bound P_{lower} and upper bound P_{upper} solutions for the static pressure as a function of the normalized void radius a/a_0.

been analyzed (see Fig. 3). The solid is initially at rest, stress and strain free, and a pressure P(t) is applied at the cavity wall.

The model has been meshed using a total of $15,000$ four-node axisymmetric reduced integration elements, CAX4R in ABAQUS notation. This number of elements results from placing 50 elements along the circumferential direction and 300 along the radial direction. The mesh shows radial symmetry in an attempt to retain the symmetry of the problem and minimize the potential interference of the mesh on the calculations. The elements size is constant along the circumferential direction whereas it decreases along the radial direction as the cavity is approached. Namely, the dimensions of the elements located at the cavity wall are: $0.3\,\mu\text{m} \times 0.23\,\mu\text{m}$ for $a_0 = 0.01\,\text{mm}$, $3\,\mu\text{m} \times 23\,\mu\text{m}$ for $a_0 = 0.1\,\text{mm}$ and $31\,\mu\text{m} \times 252\,\mu\text{m}$ for $a_0 = 1\,\text{mm}$. Small elements are required to capture the high gradients of stress and strain which arise close to the cavity. A mesh convergence study has been performed, and the time evolution of different critical output variables, namely stress, strain and cavitation velocity were compared

against a measure of mesh density until the results converged satisfactorily.

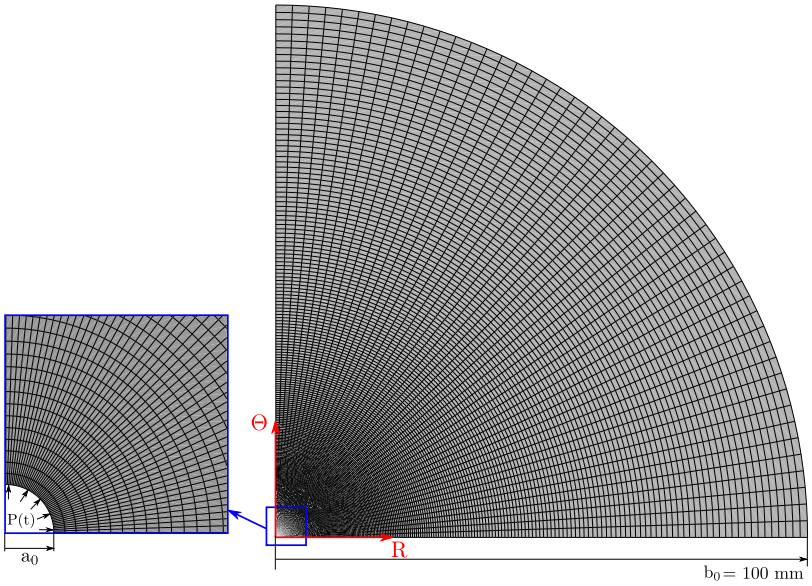

Figure 3: Axisymmetric finite element model developed to analyse dynamic spherical cavity expansion.

The set of constitutive equations describing the material behaviour presented in section 2 are implemented into the finite element code through a user subroutine. For that task, we have used the numerical scheme developed by Aranda-Iglesias et al. (2016).

5. Results and discussion

In this section we present finite element results for the spherical void expansion problem using two different loading conditions: (1) monotonically increasing pressure and (2) constant pressure. Both loading conditions, widely used in the numerical analysis of cavitation problems (Kumar et al., 2016, Rodríguez-Martínez et al., 2014), show clear evidences of the stabilizing effect played by viscosity and inertia in the expansion of the void. In selected cases, the numerical results are further rationalized with the predictions of the theoretical model described in section 3.

5.1. Loading condition 1: monotonically increasing pressure

A pressure is applied at the cavity wall at constant rate ($\dot{\mathrm{P}}$ = constant). According to Wu et al. (2003), different pressure rates represent loading conditions of different severity/intensity (impulsive loading, impact loading, shock loading ...). Figure 4 shows the applied pressure P versus the normalized void radius a/a_0 for different values of $\dot{\mathrm{P}}$. Namely, Fig. 4(a) shows data for the *purely* elastic material that results from considering only spring A and Fig. 4(b) shows results for the (full) viscoelastic constitutive model. In any case, the failure of the material is taken into account using the energy limiter in spring A. The first occurrence of failure at the cavity wall is identified with $*$ in the $\mathrm{P}-\mathrm{a}/\mathrm{a}_0$ curves. The initial cavity size is $\mathrm{a}_0 = 0.1$ mm. The theoretical solutions for the pressures corresponding to the lower and upper non-viscous quasi-static bounds ($\mathrm{P}_{\mathrm{lower}}$ and $\mathrm{P}_{\mathrm{upper}}$, see section 3.2) are also plotted. For the *purely* elastic material, since only spring A is considered, we have that $\mathrm{P}_{\mathrm{lower}} = \mathrm{P}_{\mathrm{upper}}$.

Firstly, we pay attention to Fig. 4(a). For applied pressure rates $\dot{\mathrm{P}} < 10^5$ MPa/s, the $\mathrm{P}-\mathrm{a}/\mathrm{a}_0$ curves coincide with $\mathrm{P}_{\mathrm{lower}} = \mathrm{P}_{\mathrm{upper}}$, as inertia effects play a negligible role in the void expansion process. The failure occurs at $\mathrm{a}/\mathrm{a}_0 \approx 1.6$, when applied pressure becomes higher than $\mathrm{P}^{\mathrm{cr}}_{\mathrm{lower}} \approx 2$ MPa. For applied pressure rates $\dot{\mathrm{P}} > 10^5$ MPa/s the $\mathrm{P}-\mathrm{a}/\mathrm{a}_0$ curves deviate from $\mathrm{P}_{\mathrm{lower}} = \mathrm{P}_{\mathrm{upper}}$. The cavity wall withstands a pressure larger than $\mathrm{P}^{\mathrm{cr}}_{\mathrm{lower}}$ due to the contribution

of inertia effects. The difference in pressure increases with a/a_0. Moreover, the slope of the $P - a/a_0$ curves increases with $\dot{P}$, which reveals the stabilizing effect of inertia. Note that a $P - a/a_0$ curve with slope tending to 0 represents an unstable growth of the void. The failure occurs for $a/a_0 \approx 4.3$. This value is much larger than the one corresponding to $\dot{P} < 10^5$ MPa/s. *It becomes apparent that inertia effects delay failure and improve the energy abortion capacity of the material. This is a key result of our investigation which helps to understand the performance of rubber-like materials under impact loading*.

Secondly, we focus on Fig. 4(b). For applied pressure rates $\dot{P} \leq 10^5$ MPa/s the $P - a/a_0$ curves lie within the lower and upper bound solutions. Within this range of pressure rates, the increasing pressure at the cavity wall with $\dot{P}$ is mostly caused by the effect of viscosity. Inertia effects seem to have a secondary contribution to the cavity expansion process. Note that P_{upper} does not correspond to a possible equilibrium solution but to the maximum load that can be carried by the cavity without intervention of inertia effects. Viscosity impedes to the cavity to reach an equilibrium condition for applied pressures larger than $P^{\text{cr}}_{\text{lower}}$. The cavity radius at the time of failure ($a/a_0 \approx 4.3$) is much larger than for the rate-independent material ($a/a_0 \approx 1.6$). *It becomes apparent that, in absence of meaningful inertia effects, viscosity delays failure and improves the energy absorption capacity of the material*. For applied pressure rates $\dot{P} > 10^5$ MPa/s, the $P - a/a_0$ curves run above the upper bound P_{upper}. The viscoelastic material withstands cavity pressures larger than $P^{\text{cr}}_{\text{upper}} \approx 9.5$ MPa, thanks to inertia effects. Inertia controls the void expansion process at a large extent and the $P - a/a_0$ curves for the *purely* elastic material and the rate-dependent material become similar.

Next, we analyze the role played by the initial void radius (a_0) in the cavity expansion process. While the quasi-static case is not sensitive to the initial dimensions of the cavity (Cohen and Molinari, 2015), inertial resistance to motion increases with the void size (Wu et al., 2003). The (full) viscoelastic constitutive model is used in the analysis. Figure 5 shows the applied pressure P versus a/a_0 for three different initial void radius: $a_0 = 0.01$ mm (green), $a_0 = 0.1$ mm (blue)

and $a_0 = 1$ mm (black). Results are shown for two different applied pressure rates: $\dot{P} = 10^6$ MPa/s (solid line) and $\dot{P} = 5 \cdot 10^6$ MPa/s (dotted line). These pressure rates (the greatest investigated in Fig. 4) favour that inertia effects play a role in the cavity expansion process. The $P - a/a_0$ curves are always above the upper bound solution P_{upper}. Increasing a_0 has the same effect on the $P - a/a_0$ curve that increasing $\dot{P}$. As the initial cavity radius increases, the pressure at the cavity wall and the (normalized) size of the void at the time of failure also do.

5.2. Loading condition 2: constant pressure

The pressure rises from zero to P_0 at a given rate $\dot{P}$ and then remains constant during the rest of the loading process. Figure 6 shows the growth rate of the void $\dot{a}$ versus the normalized void radius a/a_0 for different values of $\dot{P}$, P_0 and a_0. The symbol $*$ indicates the first occurrence of failure at the cavity wall. The (full) viscoelastic constitutive model is used in the calculations. Recall that, due to viscosity, the cavity cannot find an equilibrium configuration for applied pressures larger than $P^{\text{cr}}_{\text{lower}}$.

- Figure 6(a) considers $P_0 = 10$ MPa, $a_0 = 0.1$ mm and four different values of $\dot{P}$: 10^4, 10^5, 10^6 and 10^7 MPa/s. The case of a suddenly applied pressure ($\dot{P} \to \infty$) is also investigated. The value of P_0 is larger than the critical equilibrium pressure $P^{\text{cr}}_{\text{lower}}$. For $\dot{P} = 10^4$ MPa/s and $\dot{P} = 10^5$ MPa/s, the expansion velocity is an increasing function of a/a_0. As $\dot{P}$ increases the growth rate of the cavity $\dot{a}$ also does. The failure of the material occurs before the constant pressure P_0 is reached. For these two cases, the loading condition is essentially identical to the one considered in section 5.1. For $\dot{P} = 10^6$ MPa/s, $\dot{P} = 10^7$ MPa/s and $\dot{P} \to \infty$, the $\dot{a} - a/a_0$ curve increases rapidly, reaches a maximum and then decreases slowly. In absence of failure, the expansion velocity of the cavity would reach a constant value (horizontal asymptote in the graph) which identifies the steady-state cavitation regime (Rodríguez-Martínez et al., 2014). The

value of the steady-state expansion velocity is determined by P_0 and does not depend on $\dot{P}$. This is apparent from the results obtained for $\dot{P} = 10^6$ MPa/s, $\dot{P} = 10^7$ MPa/s and $\dot{P} \to \infty$, which virtually coincide for the largest values of a/a_0 reached. *The increase of inertia effects with the applied pressure rate ceases shortly after the constant pressure is reached.*

- Figure 6(b) considers $\dot{P} = 10^7$ MPa/s, $a_0 = 0.1$ mm and four different values of P_0: 4, 6, 8 and 10 MPa. Recall that all the values of P_0 are larger than the critical equilibrium pressure P^{cr}_{lower}. For $P_0 = 4$ MPa and $P_0 = 6$ MPa the $\dot{a} - a/a_0$ curves show an oscillatory response during the first stages of loading. The value of $\dot{a}$ turns from positive to negative (and vice versa) several times. The amplitude and velocity of the oscillations is gradually reduced until the steady-state cavitation regime ($\dot{a} =$ constant) is reached. For $P_0 = 8$ MPa a single *loop* is observed in the graph and $\dot{a}$ only takes negative values within a small range of the ratio a/a_0. The size of the cavity increases, almost, during the whole loading process. For $P_0 = 10$ MPa the response of the elastic ball is not oscillatory. No exceptions, the cavity size increases monotonically during loading. *Note that the value of the steady-state expansion velocity increases with P_0. The rise of the growth rate of the cavity with the applied pressure boosts the contribution of inertia effects to the expansion process.*

- Figure 6(c) considers $P_0 = 10$ MPa, $\dot{P} = 10^7$ MPa/s and three different values of a_0: 0.01, 0.1 and 1 mm. The growth rate of the void first increases, reaches and maximum and then gradually decreases until $\dot{a}$ becomes constant. Note that drop between the maximum and the steady value of $\dot{a}$ increases with the void size. Moreover, the growth rate of the void in the steady-state regime significantly increases with the void size. *The increase of the cavitation velocity with the void size leads to larger contribution of inertia effects to the expansion process.*

Figure 7 shows the failure time t_f versus the applied pressure rate $\dot{P}$ for four different values of P_0 and three different values of a_0. All the values of P_0

considered are greater than the critical equilibrium pressure P^{cr}_{lower}. The green marks $*$ indicate, in each case, the rise time, i.e. the time required to reach P_0. For a given value of P_0, the rise time decreases linearly with the applied pressure rate $\dot{P}$, as expected.

- Figure 7(a) shows results for the *purely* elastic constitutive model. Irrespective of P_0, the $t_f - \dot{P}$ curves are rather similar. For the lowest values of $\dot{P}$ considered, the failure occurs before the constant value of P_0 is reached and t_f decreases linearly with $\dot{P}$. For the greatest values of $\dot{P}$ explored the failure occurs after the constant value of P_0 is reached and t_f becomes largely independent of $\dot{P}$. As previously shown in Fig. 6(a), the pressure rate used to reach P_0 barely affects the cavity expansion process, including the failure time, in the regime of constant pressure. Moreover, irrespective of the value of P_0 considered, the size of the cavity delays failure. The delay is mild when the failure occurs before the cavity pressure becomes constant, but it is very significant when failure occurs during the regime of constant cavity pressure. It is apparent that, for the loading condition investigated in this section of the paper, the influence of inertia effects in the expansion process becomes especially relevant when the cavity pressure is constant.

- Figure 7(b) shows results for the (full) viscoelastic constitutive model. For all the cases analysed, the failure time is greater than the one corresponding to the *purely* elastic counterpart. The difference is especially significant in the loading cases in which inertia effects are less important, i.e. low values of a_0 and P_0. *In other words, the stabilizing effect of viscosity is exposed as long as inertia effects do not control the loading process.* The results for $a_0 = 0.01$ mm and $a_0 = 0.1$ mm are practically identical for all the values of P_0 and $\dot{P}$ explored. Furthermore, the results for $P_0 = 4$ MPa are virtually independent of a_0 and $\dot{P}$. In this case, unlike what happened for the purely elastic material, the failure occurs after the pressure has reached the constant cavity pressure.

6. Conclusions

In this paper we have conducted a comprehensive finite element analysis to identify the roles of viscosity and inertia in the dynamic expansion of a spherical void embedded into a deformable ball and subjected to internal pressure. The ball is modelled with a nonlinear viscoelastic constitutive theory which incorporates material failure. Numerical simulations, in which the viscosity of the constitutive model has been alternatively switched on and off, have been performed for different loading rates, applied pressures and void sizes. If the pressure at the cavity wall is greater than the critical equilibrium pressure, viscous and inertia effects play a role in the void expansion process, stabilize the material behaviour and delay failure. In a general manner, viscous effects are important as long as the cavity pressure does not exceed the upper bound of the rate-dependent material response, i.e. inertia effects become meaningful after the cavity pressure exceeds the upper bound of the rate-dependent material response. Nevertheless, the specific contribution of inertia and viscous effects to the cavity expansion process is highly dependent on the void size. Inertia effects are significantly more important as the cavity size increases.

All in all, this research has shown the need of including viscous and inertia effects in the analysis of elastomers subjected to dynamic loading conditions. This is a key outcome since elastomers are currently widely used in tires, isolation bearings, shock absorbers... and many other applications in which they are frequently subjected to shocks, blasts and impacts. In this regard, the prospective work is to extend the application of the viscoelastic constitutive model used in this paper to the aforementioned engineering problems and identify/quantify the actual contribution of viscous and inertia effects to the performance of elastomeric structures subjected to various kinds of dynamic loadings.

Acknowledgments

AF and KYV acknowledge the support received from the Israel Science Foundation, grant No. ISF-198/15.

JARM is indebted to the Ministerio de Economía y Competitividad de España (Projects EUIN2015-62556 and DPI2014-57989-P) for the financial support which enabled him to conduct part of this work.

References

ABAQUS/Explicit, 2013. Abaqus Explicit v6.13 User's Manual, version 6.13 Edition. ABAQUS Inc., Richmond, USA.

Abeyaratne, R., Horgan, C. O., 1985. Initiation of localized plane deformations at a circular cavity in an infinite compressible nonlinearly elastic medium. Journal of Elasticity 15 (3), 243–256.

Aranda-Iglesias, D., Vadillo, G., Rodríguez-Martínez, J. A., Volokh, K. Y., 2016. Modeling deformation and faliure of elastomers at high strain rates. Submitted.

Ashby, M. F., Blunt, F. J., Bannister, M., 1989. Flow characteristics of highly constrained metal wires. Acta Metallurgica 37 (7), 1847–1857.

Ball, J. M., 1982. Discontinuous equilibrium solutions and cavitation in nonlinear elasticity. Philosophical Transactions of the Royal Society of London A: Mathematical, Physical and Engineering Sciences 306 (1496), 557–611.

Bassani, J. L., Durban, D., Hutchinson, J. W., 1980. Bifurcation of a spherical hole in an infinite elastoplastic medium. Mathematical Proceedings of the Cambridge Philosophical Society 87 (02), 339–359.

Buchely, M. F., Marañon, A., 2016. Study of steady cavitation assumptions in strain-rate-sensitive solids for rigid projectile penetrations. Acta Mechanica, 1–15.

Bucknall, C. B., 1977. Toughened plastics. Springer.

Cohen, T., Durban, D., 2013. Hypervelocity cavity expansion in porous elasto-plastic solids. Journal of Applied Mechanics 80 (1), 011017.

Cohen, T., Molinari, A., 2015. Dynamic cavitation and relaxation in incompressible nonlinear viscoelastic solids. International Journal of Solids and Structures 69, 544–552.

Cristiano, A., Marcellan, A., Long, R., Hui, C.-Y., Stolk, J., Creton, C., 2010. An experimental investigation of fracture by cavitation of model elastomeric networks. Journal of Polymer Science: Part B: Polymer Physics 48 (13), 1409–1422.

Durban, D., Baruch, M., 1976. On the problem of a spherical cavity in an infinite elasto-plastic medium. Journal of Applied Mechanics 43 (4), 633–638.

Durban, D., Fleck, N. A., 1997. Spherical cavity expansion in a drucker-prager solid. Journal of Applied Mechanics 64 (4), 743–750.

Durban, D., Masri, R., 2004. Dynamic spherical cavity expansion in a pressure sensitive elastoplastic medium. International Journal of Solids and Structures 41 (20), 5697–5716.

Eckart, C., 1948. The thermodynamics of irreversible process. IV. the theory of elasticity and aaelasticity. Physical Review 73 (4), 373–382.

Faye, A., Parameswaran, V., Basu, S., 2016. Effect of notch-tip radius on dynamic brittle fracture of polycarbonate. Experimental Mechanics 56 (6), 1051–1061.

Faye, A., Parmeswaran, V., Basu, S., 2015. Dynamic cavitation and relaxation in incompressible nonlinear viscoelastic solids. Journal of the Mechanics and Physics of Solids 77, 43–60.

Fond, C., 2001. Cavitation criterion for rubber materials: A review of void-growth models. Journal of Polymer Science Part B: Polymer Physics 39 (17), 2081–2096.

Gent, A. N., 1990. Cavitation in rubber: a cautionary tale. Rubber Chemistry and Technology 63 (3), 49–53.

Gent, A. N., Lindley, P. B., 1959. Internal rupture of bonded rubber cylinders in tension. Proceedings Mathematical Physical and Engineering Sciences 249.

Henao, D., 2009. Cavitation, invertibility, and convergence of regularized minimizers in nonlinear elasticity. Journal of Elasticity 94 (1), 55–68.

Hoo Fatt, M. S., Ouyang, X., 2008. Three-dimensional constitutive equations for styrene butadiene rubber at high strain rates. Mechanics of Materials 40 (1–2), 1–16.

Horgan, C. O., Polignone, D. A., 1995. Cavitation in nonlinearly elastic solids: A review. Applied Mechanics Reviews 48 (8), 471–485.

Hou, H. S., Abeyaratne, R., 1992. Cavitation in elastic and elastic-plastic solids. Journal of the Mechanics and Physics of Solids 40 (3), 571–592.

Huang, Y., Hutchinson, J. W., Tvergaard, V., 1991. Cavitation instabilities in elastic-plastic solids. Journal of the Mechanics and Physics of Solids 39 (2), 223–241.

Hunter, S. C., Crozier, R. J. M., 1968. Similarity solution for the rapid uniform expansion of a spherical cavity in a compressible elastic-plastic solid. The Quarterly Journal of Mechanics and Applied Mathematics 21 (4), 467–486.

Kumar, A., Aranda-Iglesias, D., López-Pamies, O., 2016. Some remarks on the effects of inertia and viscous dissipation in the onset of cavitation in rubber. Journal of Elasticity.

Kundu, S., Crosby, A. J., 2009. Cavitation and fracture behavior of polyacrylamide hydrogels. Soft Matter 5 (20), 3963–3968.

Lefèvre, V., Ravi-Chandar, K., López-Pamies, O., 2015. Cavitation in rubber: an elastic instability or a fracture phenomenon? International Journal of Fracture 192 (1), 1–23.

Leonov, A. L., 1976. Nonequilibrium thermodynamics and rheology of viscoelastic polymer media. Rheologica Acta 15 (2), 85–98.

Lev, Y., Volokh, K. Y., 2016. On the cavitation in rubberlike materials. Journal of Applied Mechanics 83 (4), 044501.

López-Pamies, O., 2010. A new I_1-based hyperelastic model for rubber elastic materials. Comptes Rendus Mécanique 338 (1), 3–11.

López-Pamies, O., Idiart, M. I., Nakamura, T., 2011a. Cavitation in elastomeric solids: I a defect-growth theory. Journal of the Mechanics and Physics of Solids 59 (8), 1464–1487.

López-Pamies, O., Nakamura, T., Idiart, M. I., 2011b. Cavitation in elastomeric solids: I onset of cavitation surfaces for neo-hookean materials. Journal of the Mechanics and Physics of Solids 59 (8), 1488–1505.

Ortiz, M., Molinari, A., 1992. Effect of strain hardening and rate sensitivity on the dynamic growth of a void in a plastic material. Journal of applied mechanics 59 (1), 48–53.

Reese, S., Govindjee, S., 1998. A theory of finite viscoelasticity and numerical aspects. International Journal of Solids and Structures 35 (26–27), 3455–3482.

Rodríguez-Martínez, J. A., Cohen, T., Zaera, R., 2014. Approaching steady cavitation: The time scale in hypervelocity cavity expansion in work hardening and transformation hardening solids. International Journal of Impact Engineering 73, 43–55.

Serpooshan, V., Zokaei, S., Bagheri, R., 2007. Effect of rubber particle cavitation on the mechanical properties and deformation behavior of high-impact polystyrene. Journal of applied polymer science 104 (2), 1110–1117.

Singh, I., Guo, T. F., Murali, P., Narasimhan, R., Zhang, Y. W., Gao, H. J., 2013. Cavitation in materials with distributed weak zones: implications on

the origin of brittle fracture in metallic glasses. Journal of the Mechanics and Physics of Solids 61 (4), 1047–1064.

Singh, I., Guo, T. F., Narasimhan, R., Zhang, Y. W., 2014. Cavitation in brittle metallic glasses–effects of stress state and distributed weak zones. International Journal of Solids and Structures 51 (25), 4373–4385.

Steenbrink, A. C., Van der Giessen, E., Wu, P. D., 1997. Void growth in glassy polymers. Journal of the Mechanics and Physics of Solids 45 (3), 405–437.

Volokh, K. Y., 2007. Hyperelasticity with softening for modeling materials failure. Journal of the Mechanics and Physics of Solids 55 (10), 2237–2264.

Volokh, K. Y., 2013a. An approach to elastoplasticity at large deformations. European Journal of Mechanics A/Solids 39, 153–162.

Volokh, K. Y., 2013b. Review of the energy limiters approach to modeling failure of rubber. Rubber Chemistry and Technology 86 (3), 470–487.

Wright, T. W., Ramesh, K. T., 2008. Dynamic void nucleation and growth in solids: a self-consistent statistical theory. Journal of the Mechanics and Physics of Solids 56 (2), 336–359.

Wu, X. Y., Ramesh, K. T., Wright, T. W., 2003. The dynamic growth of a single void in a viscoplastic material under transient hydrostatic loading. Journal of the Mechanics and Physics of Solids 51 (1), 1–26.

Zimberlin, J. A., Sanabria-DeLong, N., Tewa, G. N., Crosby, A. J., 2007. Cavitation rheology for soft materials. Soft Matter 3 (6), 763–767.

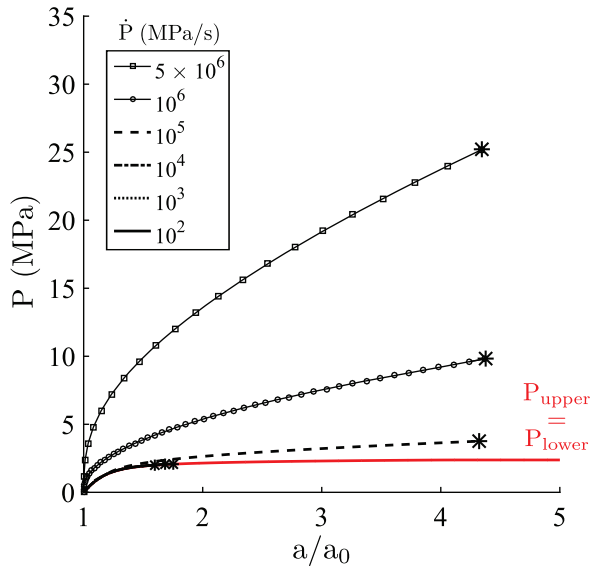

(a)

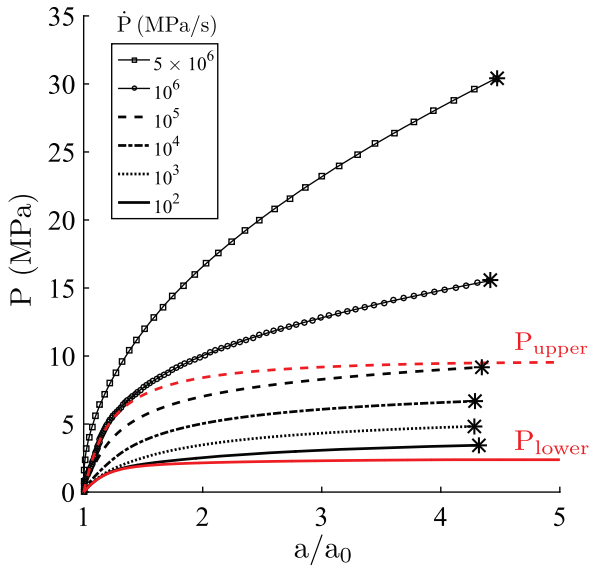

(b)

Figure 4: Applied pressure P versus the normalized void radius a/a_0 for different values of $\dot{P}$. (a) *Purely* elastic constitutive model and (b) viscoelastic constitutive model. The symbol $*$ indicates the first occurrence of failure (i.e. $\psi_A = \psi_A^f$) at the cavity wall. The initial cavity size is $a_0 = 0.1$ mm.

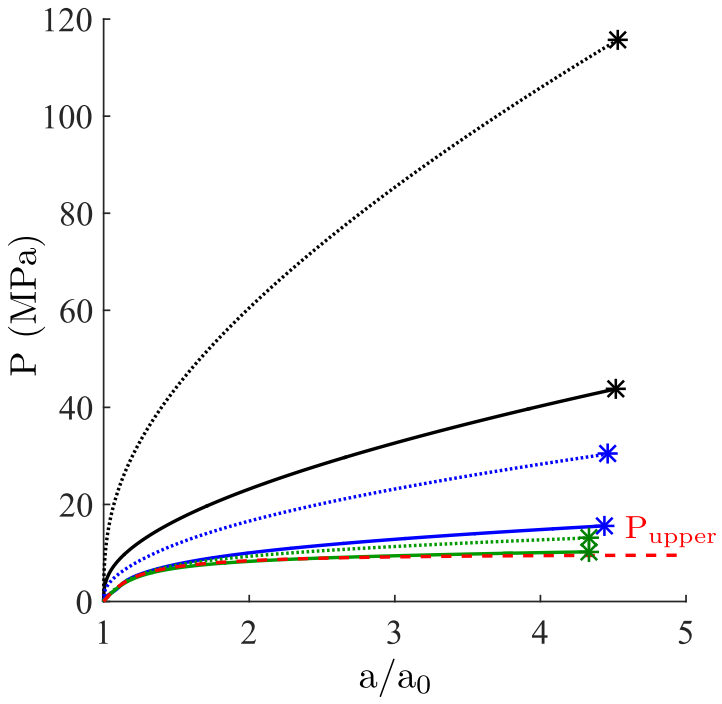

Figure 5: Applied pressure P versus the normalized void radius a/a_0 for three different initial void radius: $a_0 = 0.01$ mm (green), $a_0 = 0.1$ mm (blue) and $a_0 = 1$ mm (black). Results are shown for two different applied pressure rates: $\dot{P} = 10^6$ MPa/s (solid line) and $\dot{P} = 5 \cdot 10^6$ MPa/s (dotted line).

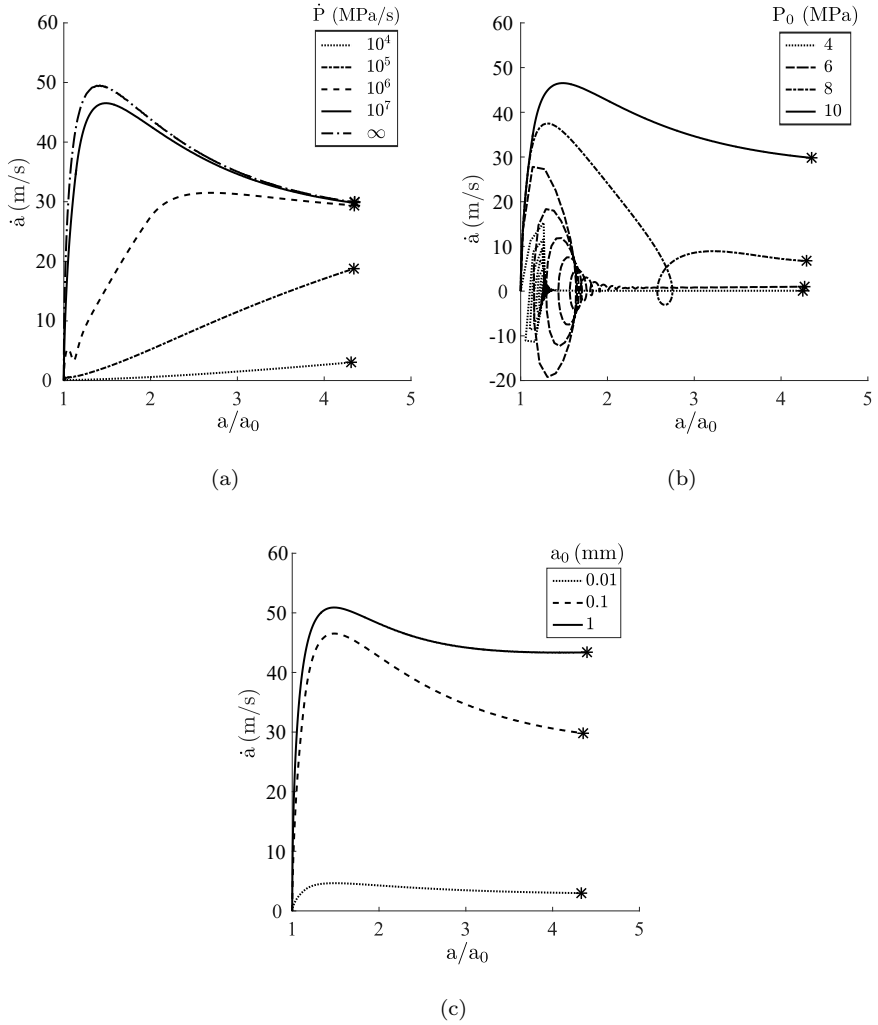

Figure 6: Growth rate of the void $\dot{a}$ versus the normalized void radius a/a_0. (a) We consider $P_0 = 10$ MPa, $a_0 = 0.1$ mm and four different values of $\dot{P}$: 10^4, 10^5, 10^6 and 10^7 MPa/s. The case of $\dot{P} \to \infty$ is also taken into account. (b) We consider $\dot{P} = 10^7$ MPa/s, $a_0 = 0.1$ mm and four different values of P_0: 4, 6, 8 and 10 MPa. (c) We consider $P_0 = 10$ MPa, $\dot{P} = 10^7$ MPa/s and three different values of a_0: 0.01, 0.1 and 1 mm.

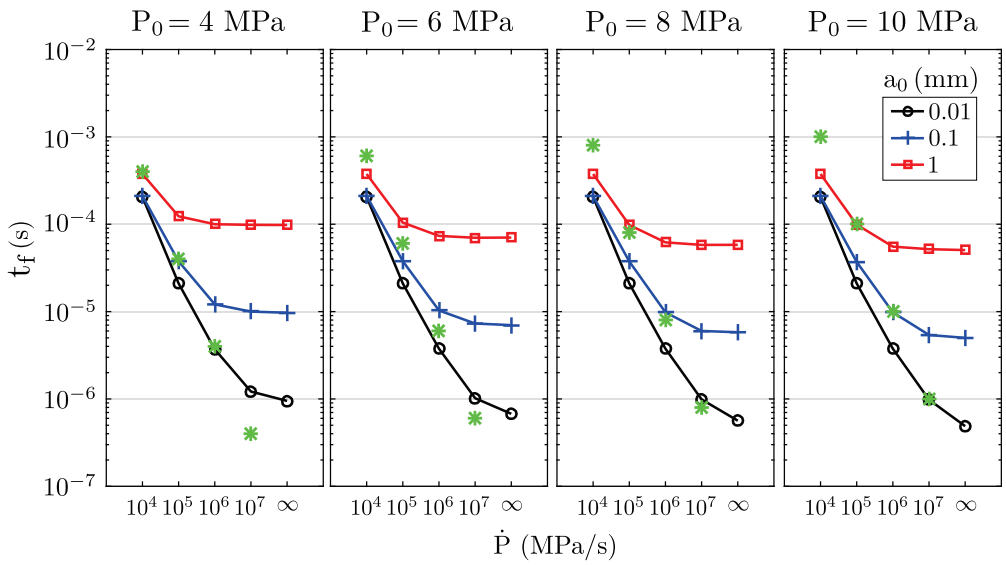

(a)

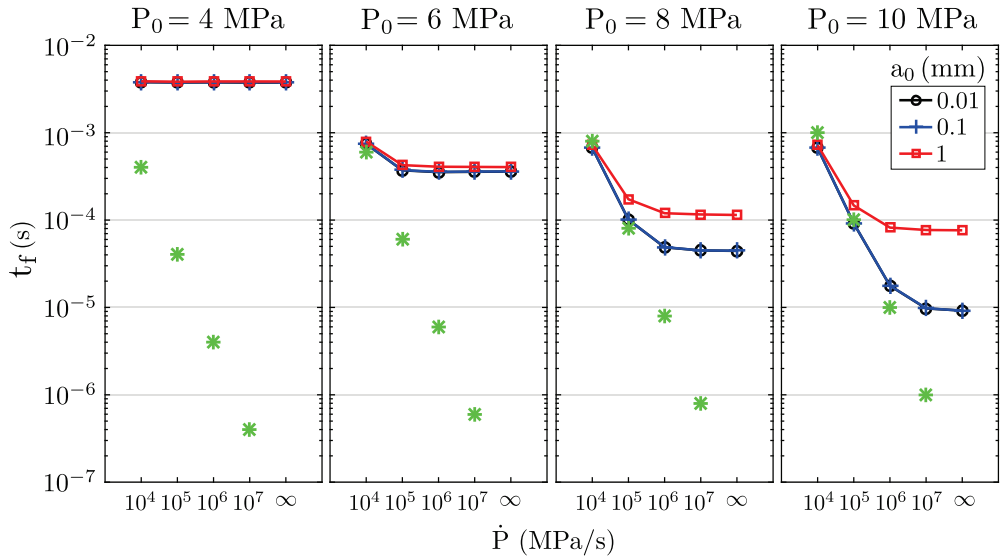

(b)

Figure 7: Failure time t_f versus the applied pressure rate $\dot{P}$ for (a) *purely* elastic and (b) viscoelastic materials. Four different values of P_0 are considered: 4, 6, 8 and 10 MPa. Three different values of a_0 are considered: 0.01, 0.1 and 1 mm.